

# Configuration Maintenance of Inflated Membrane Structures Using SMA Film Actuators

Jin-Ho Roh<sup>1</sup> and In Lee<sup>2</sup>

**Abstract:** A methodology to maintain the configuration of inflated membrane structures using shape memory alloy (SMA) film actuator is numerically investigated. The two-dimensional incremental formulation of the SMA constitutive model is developed. New parameters related to the thermodynamic energy equation are introduced to describe more general behaviors of the SMA film. With numerical algorithm of wrinkling and SMAs, the interactions between the inflated membrane structure and the SMA film are investigated by using a finite element program. The effectiveness of SMA film to control the configuration of an inflated membrane structure is examined. To demonstrate surface configuration control, two inflatable membrane structures, each with SMA film are used: (1) an inflatable boom similar to a strut supporting structure and (2) an inflatable reflector, which is comprised of two inflated membranes and torus supporting structures.

**Keyword:** Inflatable structures, Wrinkling, SMA film.

## 1 Introduction

An inflatable structure belongs to membrane structures that usually imply thin materials and low modulus. Membrane structures are either in tensioned-planar or inflated-curved configurations. Compared to traditional mechanical systems, inflatable structures have several advantages, including much lower costs, lower weights and lower packaging volumes as well as more fa-

vorable thermal gradients and damping characteristics. These structures can be packaged into smaller volumes, eventually reduces an overall space mission cost and the launch vehicle size requirements. However, surface distortion of the structure may be easily induced by boundary conditions, thickness variations, wrinkling, thermal distortions, membrane inflation level, and surface roughness in the membrane material itself. Therefore, the reliable maintenance of the surface precision during the mission life is one of the most important technologies for the feasible use of inflatable structures. The basic approach for maintaining the desired surface accuracy during operation is to integrate an actuator and sensors into the surface, as well as into the support structure of the inflatable structure system. Traditional methods to maintain the surface accuracy of an inflatable structure will increase the weight and maintenance cost of the structures either actively or passively. However, by using developed intelligent materials and embedded system hardware, the technology of maintaining surface precision could be achieved for the potential development of inflatable structures. The concept of using smart materials to maintain the surface accuracy of inflatable structures was proposed by Salama et al. (1994). They studied a potentially lightweight and simple technique to correct local aberrations in the shape of inflatable structures by shrinking or stretching sections of the membrane or support structure. They employed piezoelectric elements in the construction of the membrane and support structure. Many researchers have also performed the vibration control of inflatable structures using smart materials. Wagner et al. (2000) developed a membrane mirror with a PVDF (polyvinylidene fluoride) film to maintain a stable imaging platform. Lewis and Inman (2001)

---

<sup>1</sup> Research Engineer, Department of Mechanical Engineering, The Pennsylvania State University, USA, jzr13@psu.edu

<sup>2</sup> Corresponding author. Department of Aerospace Engineering, Korea Advanced Institute of Science and Technology, Korea, inlee@kaist.ac.kr

discussed the structural dynamics and vibration suppression of an inflatable torus with piezoelectric actuators. However, there were many difficulties involved with controlling the shape or vibration of inflatable structures using piezoelectric materials. One of the limitations of a piezoelectric actuator was the amount of force it can exert. In addition, active control (both position control and vibration suppression) lost authority because of the extreme flexibility of an inflatable structure's skin. Moreover, the choice of applicable sensing and actuation materials suitable to inflatable structures was somewhat limited because of the need for these material actuation and sensing systems to be able to fold up prior to deployment. More recently, research has been directed toward demonstrating actuator architectures and approaches suitable for controlling very thin inflatable structures. Example work, including active seam bonded onto membranes, was presented by Jenkins and Schur (2002). This concept mimicked the wing structure of a bat in bones and tendons of a bat together deploy the wing and keep the skin aerodynamically configured. Approaches involving deployment / surface actuation (mostly by the use of SMA and PZT) have also been presented [Flint and Denoyer (2003)]. Duvvuru et al. (2003) reported on the possibility of active seams consisting of integrated actuators and sensors, which would allow for controlled deployment of the inflatable structures. However, there remain many obstacles to apply smart materials to inflatable systems. The interactions between the sensor / actuator and the inflated membrane structures should be investigated with an improved modeling technique. In addition, a detailed analysis is required to truly understand and determine the effectiveness of position and vibration control of the inflatable structure.

In this study, a methodology to maintain the shape configuration of inflated membrane structures with an SMA film actuator is numerically investigated. To understand the nonlinear behaviors of inflated membrane structures due to wrinkling, a numerical model of inflated membrane structure applying the Stein-Hedgepeth membrane theory is considered. To predict the thermomechanical

behaviors of an SMA film, the two-dimensional incremental formulation of the SMA constitutive model is proposed by modifying the Lagoudas model into plane stress problems. New parameters related to the thermodynamic energy equation are introduced to describe more general behaviors of the SMA film. For the numerical results of the inflatable structure and the SMA film, ABAQUS is used as the finite element solver. The numerical algorithms of wrinkling and SMAs are developed via a user subroutine (UMAT) supported by ABAQUS. The simple methodology to shrink or stretch sections of the membrane or the support structure is applied. By coupling both numerical algorithms of wrinkling and the SMA film, the interactions between the inflatable structure and SMA film actuator are investigated. Furthermore, the effectiveness of SMA film to control the configuration of inflated membrane structures is examined. For the demonstration of surface configuration control, two inflatable membrane structures using SMA film are considered: (1) an inflatable boom similar to a strut supporting structure and (2) an inflatable reflector, which is comprised of two inflated membranes and torus supporting structures.

## 2 Nonlinear Behaviors of Inflated Membrane Structures

### 2.1 Membrane model with wrinkling

In order to consider wrinkling of membrane, the wrinkling model of Stein and Hedgepeth (1961) is applied. This wrinkle theory applies to membranes that are elastic, isotropic, have no bending stiffness and cannot carry compressive stress. If both principal stresses are tensile then the membrane is taut. If both principal stresses are zero, then the membrane is slack. However, if one principal stress (minor) is zero and the other (major) is tensile, then the membrane wrinkles. A numerical algorithm that retains the nonlinear wrinkle model may be expressed as:

$$\boldsymbol{\sigma} = \mathbf{D}\boldsymbol{\varepsilon} \quad (1)$$

where,  $\boldsymbol{\sigma} = \{\sigma_{xx}, \sigma_{yy}, \tau_{xy}\}^T$ ,  $\boldsymbol{\varepsilon} = \{\varepsilon_{xx}, \varepsilon_{yy}, \gamma_{xy}\}^T$  and  $\mathbf{D}$  is a local "equivalent elasticity" matrix that

relates stresses  $\boldsymbol{\sigma}$  and elastic strain  $\boldsymbol{\varepsilon}$  within a membrane element. A useful algorithm for choosing the  $\mathbf{D}$  matrix, the Stress-Strain Criteria is used [Kang and Im (1999) and Woo et al. (2004)]:

Stress-Strain Criteria

$$\sigma_2 > 0 : \text{taut} \quad (2a)$$

$$\varepsilon_1 \leq 0 : \text{slack} \quad (2b)$$

$$\varepsilon_1 > 0 \text{ and } \sigma_2 \leq 0 : \text{wrinkled} \quad (2c)$$

where  $\sigma_2$  and  $\varepsilon_1$  are a minor principal stress and a major principal strain, respectively. The effective elasticity matrix at each membrane state can be expressed as follows:

$$\mathbf{D}_{Taut} = \frac{E}{1-\nu^2} \begin{bmatrix} 1 & \nu & 0 \\ \nu & 1 & 0 \\ 0 & 0 & \frac{1-\nu}{2} \end{bmatrix} \quad (3a)$$

$$\mathbf{D}_{Slack} = \begin{bmatrix} 0 & 0 & 0 \\ 0 & 0 & 0 \\ 0 & 0 & 0 \end{bmatrix} \quad (3b)$$

$$\mathbf{D}_{Wrinkled} = \frac{E}{4} \begin{bmatrix} 2(1+P) & 0 & Q \\ 0 & 2(1-P) & Q \\ Q & Q & 1 \end{bmatrix} \quad (3c)$$

where,  $P = \cos(2\alpha)$ ,  $Q = \sin(2\alpha)$ , and  $\alpha$  is the principal angle. The taut matrix (Eq. 3a) follows the linear elastic isotropic material constitutive formulation. The slack matrix (Eq. 3b) formulation is based upon the assumption that no stress is formed in a slack region. The wrinkled matrix (Eq. 3c) is formulated from the constitutive relations by using the variable Poisson's ratio [Stein and Hedgepeth (1961)].

The numerical analysis involves nonlinear stress-strain behavior, so that an iterative solution is required. The resulting model is analyzed with the same loads and the process is repeated until no compressive stresses remain in the membrane. To simulate a wrinkling phenomenon, the numerical algorithm of wrinkling is implemented via a user subroutine (UMAT) supported by the ABAQUS [Hibbitt et al. (2003)] finite element program (Fig. 1). In this model, membrane states of taut, wrinkled and slack are calculated at each load step by using Stress-Strain Criteria (Eqs. 2a-c) and the Stein-Hedgepeth wrinkling model (Eqs. 3a-c).

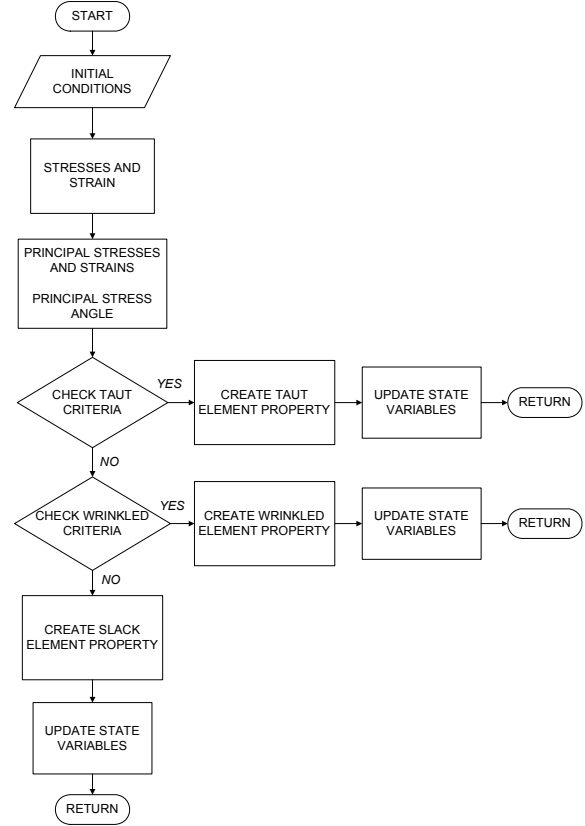


Figure 1: Numerical algorithm of wrinkling

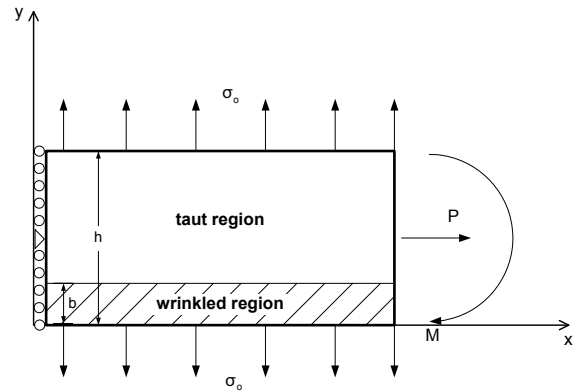


Figure 2: Flat stretched membrane subjected to pure bending moment

To verify the numerical algorithm of wrinkling, the pure bending of a stretched rectangular membrane is considered. A rectangular membrane that is uniformly pretensioned with normal stress  $\sigma_0$  in the  $y$ -direction and with axial load  $P = \sigma_0 \cdot t \cdot h$  in the  $x$ -direction is shown in Fig. 2, where  $t$  is

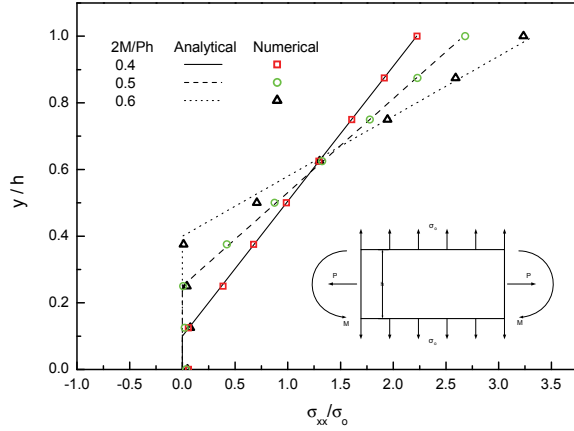


Figure 3: Normal stress  $\sigma_{xx}/\sigma_o$  vs. vertical position  $y/h$  for pure bending of flat stretched membrane

the thickness of the membrane. Subsequently, an in-plane bending moment,  $M$  is applied along the right edge. As  $M$  increases, a band of vertical wrinkles of width  $b$  forms along the lower edge of the membrane as the normal strain  $\epsilon_{xx}$  in this region becomes compressive. This band of wrinkles is described as [Miller et al. (1985)]:

$$\frac{b}{h} = \begin{cases} 0, & \frac{M}{Ph} < \frac{1}{6} \text{ (taut)} \\ \frac{3M}{Ph} - \frac{1}{2}, & \frac{1}{6} \leq \frac{M}{Ph} < \frac{1}{2} \text{ (partially wrinkled)} \end{cases} \quad (4)$$

The stress within the membrane can be expressed as:

$$\frac{\sigma_{xx}}{\sigma_o} = \begin{cases} \frac{2(\frac{y}{h} - \frac{b}{h})}{(1 - \frac{b}{h})^2}, & \frac{b}{h} < \frac{y}{h} \leq 1 \\ 0, & 0 \leq \frac{y}{h} \leq \frac{b}{h} \end{cases} \quad (5a)$$

$$\frac{\sigma_y}{\sigma_o} = 1 \quad (5b)$$

$$\frac{\tau_{xy}}{\tau_o} = 0 \quad (5c)$$

A finite element model is created using  $16 \times 8$  membrane elements (M3D4), supported by ABAQUS [Hibbitt et al. (2003)]. The edge constraints adopted along the left edge of the model consist of the requirement that  $u_x = 0$ , where  $u_x$  is the nodal displacement in the x-direction. All nodal points along this edge are free to move in the y-direction except the node at the center of

this edge, which is constrained such that  $u_y = 0$ . The upper and lower edges of the model are subjected to vertical tensile loads at each node. The magnitude of these loads is determined such that they are equivalent to a uniform tensile normal stress of  $\sigma_o$  along each edge. The right edge of the membrane model is attached to a finite element model of a very stiff beam upon which the external loads  $P$  and  $M$  are applied. The attachment between the membrane and beam models is accomplished by requiring continuity of displacements in the x-direction at each node. However, the displacements in the y-direction for nodes belonging to the membrane are not required to be attached the beam, except at the node at the center of the edge. Numerical results are generated by first applying the pretensioning forces  $P$  and  $\sigma_o$ . After the equilibrium states for the pretensioned membrane is obtained, a bending moment  $M$  is applied in small increments to the stiff beam. An iterative solution for equilibrium displacements is generally required after each increment of bending moment.

A comparison of analytical and numerical results for  $\sigma_{xx}$  vs.  $y$  for three different levels of bending moment is shown in Fig. 3. The analytical results are generated by Eqs. (5a-c), and the numerical results correspond to  $\sigma_{xx}$  at each nodal points. As can be seen, there are in a good agreement between the analytical and present results, even for the highly nonlinear region. The results indicate that about 40% of the membrane surface is a wrinkled region for  $2M/Ph = 0.6$ .

## 2.2 Inflated membrane boom subjected to tip force

To investigate the nonlinear behaviors of inflated membrane structure due to wrinkling, the inflated membrane boom is numerically modeled, and the results are compared with experimental data of Yoo et al. (2007). A numerical model for an inflated membrane boom is shown in Fig. 4.

The rigid body constraint is applied to the upper edge. When the boom structure is pressurized, the membrane is tensioned longitudinally as well as laterally. Considering the pressure load to the upper end cap surface, the stretching

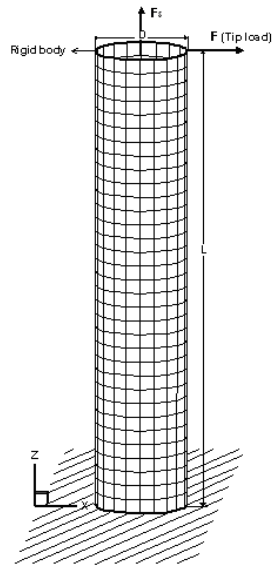


Figure 4: An inflated membrane boom

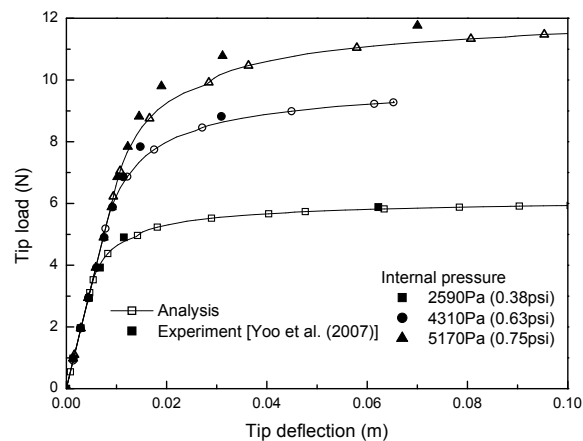


Figure 5: Load-deflection curves for various internal pressure

force ( $F_s$ ) is applied. The thickness  $t$ , Young's modulus  $E$ , and Poisson's ratio  $\nu$  of the Kapton film is  $30\mu\text{m}$ ,  $3\text{GPa}$  and  $0.34$ , respectively. In the finite element analysis, the inflated membrane boom model with 660 membrane elements (M3D4) is used, whereby membrane states, such as taut, slack and wrinkled, are calculated at each load step by using the Stein-Hedgepeth wrinkling model (Eqs. 3a-c). Considering computational time, a mesh having 33 elements in the length direction and 20 around the circumference is applied.

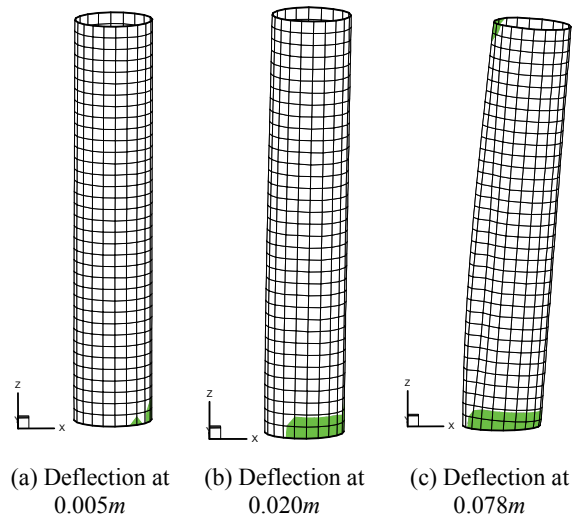


Figure 6: Deformed shapes with wrinkled area (internal pressure,  $P=2,590\text{Pa}$ )

Consequently, the load and deflection curves for several internal pressures are shown in Fig. 5 in the case of the slenderness ratio  $2L/D = 10.5$  (length,  $L=1\text{m}$  and diameter,  $D=0.19\text{m}$ ). As shown in Fig. 5, there are very good correlations between analysis and experimental results [Yoo et al. (2007)]. By increasing internal pressure, the critical load to initiate collapse is also increased. The expansion of the wrinkling area and the deformed shape of the inflated membrane boom are investigated. As shown in Fig. 6, the wrinkled area develops near the bottom region in the circumferential direction, according to deflection increase. As the tip deflects  $0.078\text{m}$ , the inflated membrane boom collapses (Fig. 6(c)). The wrinkled state can be seen not only at the bottom side area but also at the top side opposite to the tip load. The wrinkling is generated at the top side by a compressive load due to the rotation of the top rigid line. The membrane elements at the bottom region collapse due to wrinkling extension. The right side remains almost straight, and the tip deflection is increased due to the wrinkled elements at the bottom side area. The left side line is curved and the mid section of the inflated membrane boom cannot maintain a perfect cylindrical shape. Therefore, the wrinkled elements cannot sustain the applied load any longer and simply play the role of a hinge.

### 3 Thin Film Shape Memory Alloys

#### 3.1 Constitutive equations for thin film SMA

The two-dimensional incremental formulation for the SMA constitutive model is proposed to predict the thermomechanical behaviors of SMA film. For two-dimensional problems, the general expressions derived by Lagoudas [Qidwai and Lagoudas (2000)] have to be modified. The model consists of three equations: (1) the constitutive equations, (2) the transformation equation, and (3) the transformation surface equation. The constitutive equation can be expressed as describing the time rate of change of strain,  $\dot{\boldsymbol{\epsilon}}$ , in terms of the increments of stress,  $\dot{\boldsymbol{\sigma}}$ , temperature,  $\dot{T}$ , and martensite fraction,  $\dot{\xi}$ , i.e.,

$$\dot{\boldsymbol{\epsilon}} = \mathbf{S}\dot{\boldsymbol{\sigma}} + \boldsymbol{\alpha}\dot{T} + \mathbf{Q}\dot{\xi} \quad (6)$$

where,  $\mathbf{S} = \mathbf{C}^{-1}$  is the elastic compliance matrix,  $\boldsymbol{\alpha}$  is the thermal expansion coefficient vector and the vector  $\mathbf{Q}$  indicates the relationships between the time rate of change of strain and martensite fraction. The stress, strain, thermal expansion, and compliance matrix can be expressed as the condition of plane stress.

$$\begin{aligned} \dot{\boldsymbol{\sigma}} &= [\dot{\sigma}_{xx}, \dot{\sigma}_{yy}, \dot{\sigma}_{xy}]^T, \\ \dot{\boldsymbol{\epsilon}} &= [\dot{\epsilon}_{xx}, \dot{\epsilon}_{yy}, \dot{\epsilon}_{xy}]^T, \\ \boldsymbol{\alpha} &= [\alpha_{xx}, \alpha_{yy}, \alpha]_T, \\ \mathbf{S} &= \begin{bmatrix} 1/E & -\nu/E & 0 \\ -\nu/E & 1/E & 0 \\ 0 & 0 & 2(1+\nu)/E \end{bmatrix} \end{aligned} \quad (7)$$

The other term in Eq. (6) is defined by,

$$\mathbf{Q} = \Delta\mathbf{S}\boldsymbol{\sigma} + \Delta\boldsymbol{\alpha}(T - T_o) + \boldsymbol{\Lambda} \quad (8)$$

The prefix  $\Delta$  in Eq. (8) represents the difference of a quantity between the martensite and austenite phases as follows:

$$\Delta\mathbf{S} = \mathbf{S}^M - \mathbf{S}^A, \Delta\boldsymbol{\alpha} = \boldsymbol{\alpha}^M - \boldsymbol{\alpha}^A \quad (9)$$

Where superscript  $A$  and  $M$  stands for the austenite phase and the martensite phase, respectively.  $\boldsymbol{\Lambda}$  is the transformation strain direction and is assumed on the basis of the flow rule in the plasticity

theory to have the following form:

$$\boldsymbol{\Lambda} = \begin{cases} \frac{H}{2\bar{\sigma}^{eff}} [(2\sigma_{xx} - \sigma_{yy}), (-\sigma_{xx} + 2\sigma_{yy}), 3\sigma_{xy}]^T, & \dot{\xi} > 0 \\ \frac{H}{\bar{\epsilon}^{t-r}} [\boldsymbol{\epsilon}_{xx}^{t-r}, \boldsymbol{\epsilon}_{yy}^{t-r}, \boldsymbol{\epsilon}_{xy}^{t-r}]^T, & \dot{\xi} < 0 \end{cases} \quad (10)$$

where  $H$  is the maximum uniaxial transformation strain,  $\boldsymbol{\epsilon}^{t-r}$  is the transformation strain at the reversal of phase transformation and

$$\begin{aligned} \bar{\sigma}^{eff} &= \sqrt{\sigma_{xx}^2 + \sigma_{yy}^2 - \sigma_{xx}\sigma_{yy} + 3\sigma_{xy}^2}, \\ \bar{\epsilon}^{t-r} &= \sqrt{\frac{2}{3}\boldsymbol{\epsilon}^{t-r} \cdot \boldsymbol{\epsilon}^{t-r}} \end{aligned} \quad (11)$$

The following transformation equation relates the time rate of change of the martensite fraction to the transformation strain,  $\dot{\boldsymbol{\epsilon}}^t$ :

$$\dot{\boldsymbol{\epsilon}}^t = \boldsymbol{\Lambda}\dot{\xi} \quad (12)$$

The following transformation surface equation determines the onset of the forward (austenite to martensite) and reverse phase transformation (martensite to austenite):

$$\begin{aligned} \boldsymbol{\sigma}\boldsymbol{\Lambda} + \frac{1}{2}\boldsymbol{\sigma}\Delta\mathbf{S}\boldsymbol{\sigma} + \Delta\boldsymbol{\alpha}\boldsymbol{\sigma}(T - T_o) \\ + \rho\Delta c \left[ (T - T_o) - T \ln\left(\frac{T}{T_o}\right) \right] + \rho\Delta s_o T - \frac{\partial f}{\partial \xi} \\ - \rho\Delta u_o = \pm Y^* \end{aligned} \quad (13)$$

where  $\rho$ ,  $c$ ,  $s_o$  and  $u_o$  is the mass density, specific heat, specific entropy, specific internal energy at the reference state, respectively. The plus sign on the right hand side of Eq. (13) is used for the forward phase transformation while the minus sign is used for the reverse transformation. Note that the material constant  $Y^*$  is the measure of internal dissipation due to phase transformation and can be interpreted as the threshold value of the transformation surface for the onset of the phase transformation.

Transformation function can be defined in terms of the transformation surface equation as follows:

$$\Phi = \begin{cases} \pi - Y^*, & \dot{\xi} > 0 \\ -\pi - Y^*, & \dot{\xi} < 0 \end{cases} \quad (14)$$

The transformation function plays a role similar to the yield function in the plasticity theory. For the transformation theory, an additional constraint on martensite fraction  $\xi$  must be satisfied. Constraints on the evolution of the martensite fraction are expressed as

$$\begin{aligned} \dot{\xi} &\geq 0, & \Phi(\sigma, T, \xi) &\leq 0, & \Phi \dot{\xi} &= 0 \\ \dot{\xi} &\leq 0, & \Phi(\sigma, T, \xi) &\leq 0, & \Phi \dot{\xi} &= 0 \end{aligned} \quad (15)$$

The inequality constraints on  $\Phi(\sigma, T, \xi)$  are referred to as the transformation condition and regarded as a constraint on the state variables' admissibility. For  $\Phi < 0$ , Eq. (15) requires  $\dot{\xi} = 0$  and an elastic response is obtained. On the other hand, the forward-phase transformation (austenite to martensite) is characterized by  $\Phi = 0$  and  $\dot{\xi} > 0$ , while the reverse-phase transformation (martensite to austenite) is characterized by  $\Phi = 0$  and  $\dot{\xi} < 0$ .

In the numerical implementation of the SMA constitutive model, the tangent stiffness and the stress at each integration point of all elements should be updated in each iteration for given increments of strain and temperature. The relationship between stress and strain and temperature increments can be expressed by,

$$\dot{\boldsymbol{\sigma}} = \mathbf{L}\dot{\boldsymbol{\varepsilon}} + \mathbf{l}\dot{T} \quad (16)$$

where the tangent stiffness  $\mathbf{L}$  and the tangent thermal moduli  $\mathbf{l}$  are defined as

$$\begin{aligned} \mathbf{L} &= \left( \mathbf{S} - \frac{\mathbf{Q} \times \frac{\partial \Phi}{\partial \boldsymbol{\sigma}}}{\frac{\partial \Phi}{\partial \xi}} \right)^{-1}, \\ \mathbf{l} &= \mathbf{S}^{-1} \times \left( \mathbf{Q} \cdot \frac{\frac{\partial \Phi}{\partial T} - \frac{\partial \Phi}{\partial \boldsymbol{\sigma}} \times \mathbf{S}^{-1} \times \boldsymbol{\alpha}}{\frac{\partial \Phi}{\partial \xi} - \frac{\partial \Phi}{\partial \boldsymbol{\sigma}} \times \mathbf{S}^{-1} \times \mathbf{Q}} - \boldsymbol{\alpha} \right) \end{aligned} \quad (17)$$

The ABAQUS [Hibbitt et al. (2003)] finite element program has been utilized with a user subroutine, UMAT [Roh et al. (2006)]. The flow chart of the SMA constitutive equation for the UMAT subroutine is illustrated in Fig. 7. With state variables such as  $\boldsymbol{\sigma}$ ,  $\boldsymbol{\varepsilon}$ ,  $\boldsymbol{\varepsilon}^l$ ,  $T$  and  $\xi$ , the transformation function is determined whether the phase transformation of SMAs occurs or not.

Under the condition of phase transformation, the increment of martensite fraction is calculated by

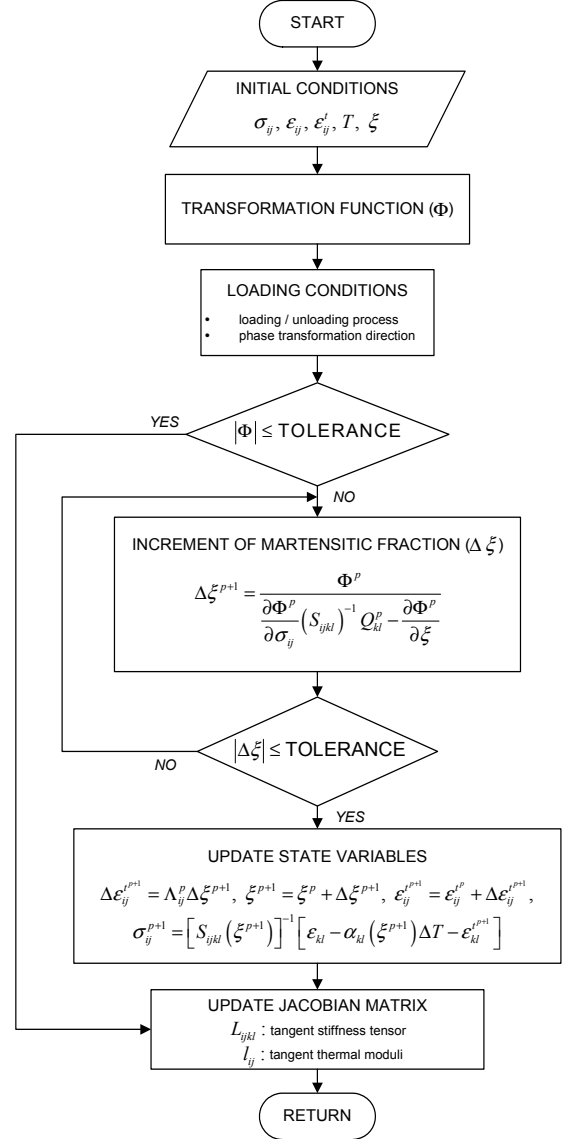


Figure 7: Algorithm for the SMA constitutive equation

using the Newton-Raphson iteration method. Finally, the increment of state variables for given strain and temperature increments can be calculated. With the updated state variables, the tangent stiffness tensor and the tangent thermal moduli are updated for the next increments of strain and temperature.

### 3.2 Thermomechanical behaviors of SMA film

The numerical results of thermomechanical behaviors of the SMA film are compared with ex-

perimental results of LExcellent et al. (1998). The dimension of the SMA film specimen is 1mm (width)  $\times$  5mm (length)  $\times$  0.006mm (thickness). For the numerical model of the SMA, 10  $\times$  4 membrane elements (M3D4) supported by ABAQUS [Hibbitt et al. (2003)] are used. The thermomechanical properties measured by LExcellent et al. (1998) are summarized in Table 1.

The critical stresses and the stress influence coefficients  $\left(\frac{d\sigma}{dT}\right)^M$  and  $\left(\frac{d\sigma}{dT}\right)^A$  of the SMA film are presented in Fig. 8. The stress influence coefficients are different for the forward and reverse phase transformations. However, Lagoudas [Qidwai and Lagoudas (2000)] simply derived the equation of SMAs and simulated for the case of  $\left(\frac{d\sigma}{dT}\right)^M = \left(\frac{d\sigma}{dT}\right)^A$ . We have therefore proposed new strain hardening parameters, and we independently define the effective specific entropy difference for forward and reverse phase transformations as follows:

Table 1: Material properties of SMA film

Moduli, Poisson's ratio, Thermal expansion	$E^A = 40.0 \times 10^9 Pa$ $E^M = 30.0 \times 10^9 Pa$ $\nu^A = \nu^M = 0.34$ $\alpha^A = 22 \times 10^{-6}/K$ $\alpha^M = 10 \times 10^{-6}/K$
Transformation temperatures	$A^{of} = 321.0K$ $A^{os} = 312.0K$ $M^{os} = 240.0K$ $M^{of} = 218.0K$
Transformation constants	$\left(\frac{d\sigma}{dT}\right)^A = 13.845 \times 10^6 Pa/K$ $\left(\frac{d\sigma}{dT}\right)^M = 4.212 \times 10^6 Pa/K$
Maximum transformation strain	$H = 0.04$

$$\rho\Delta s_o^A = -H \left(\frac{d\sigma}{dT}\right)^A, \quad (18)$$

$$\rho\Delta s_o^M = -H \left(\frac{d\sigma}{dT}\right)^M$$

Based on Eq. (18), transformation strain harden-

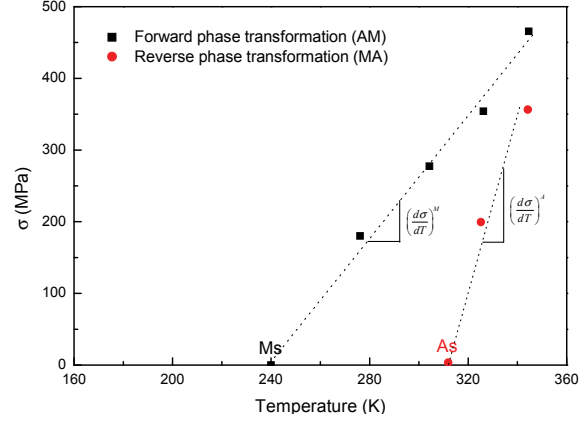


Figure 8: The temperature dependence of critical stress for inducing forward transformation and reverse transformation

ing material constants can be derived as follows:

$$\gamma = \frac{1}{2}\rho\Delta s_o^M M^{os} + \rho\Delta s_o^A A^{of}, \quad (19)$$

$$\rho b^A = -\rho\Delta s_o^A (A^{of} - A^{os}),$$

$$\rho b^M = -\rho\Delta s_o^M (M^{os} - M^{of})$$

Also, the measure of internal dissipation due to phase transformation,  $Y^*$  is induced as

$$Y^* = -\frac{1}{2}\rho\Delta s_o^A \times A^{of} + \frac{1}{2}\rho\Delta s_o^M \times M^{os}$$

$$+ \frac{1}{4}\rho\Delta s_o^M (M^{os} - M^{of}) - \frac{1}{4}\rho\Delta s_o^A (A^{of} - A^{os}) \quad (20)$$

Figure 9 shows uniaxial stress-strain curves at various temperatures, in comparison with experimental results [LExcellent et al. (1998)]. Figure 9 shows that very good agreements between the analysis and experimental results. To estimate the performance of an SMA thin film actuator, the hysteresis loop of recovery stress with respect to temperature variation is shown in Fig. 10. SMA film is restrained during the phase transformation induced by the heating process, so that a large recovery stress is generated by the shape memory effect. The recovery stress is decreased until  $A^{os}$  (312K) due to thermal expansion effect. After the austenite finish temperature, defined differently depending on initial strain, the recovery

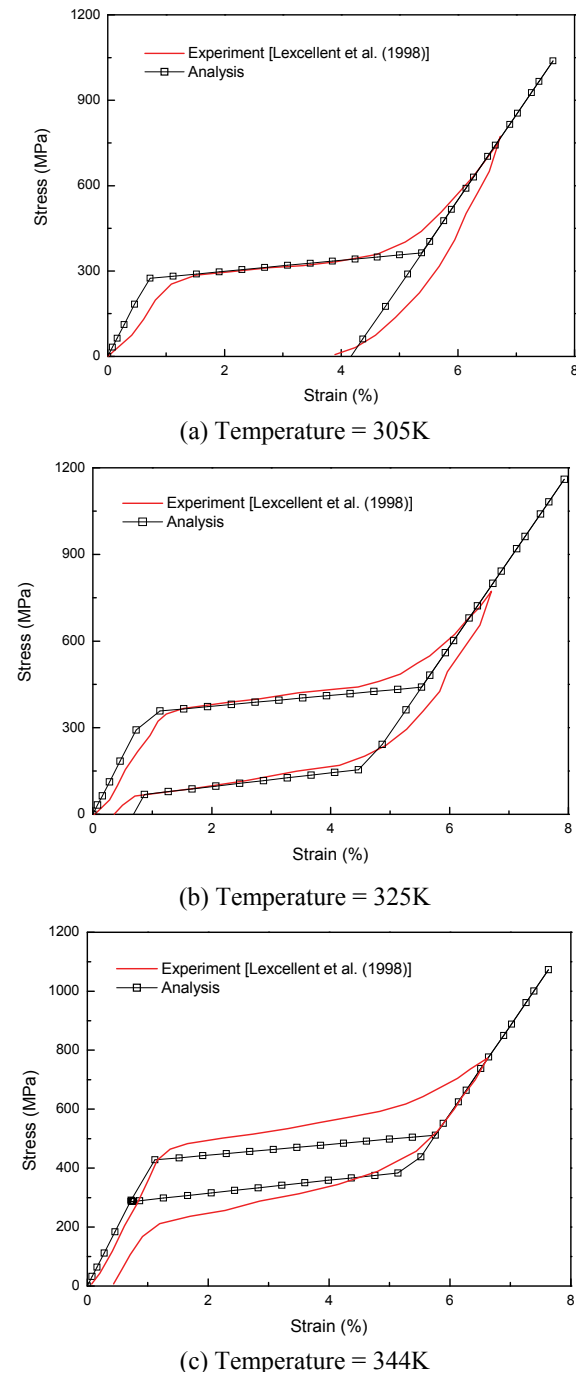


Figure 9: The stress-strain curves at various temperatures

stress should decrease again due to the thermal expansion effect. The reverse phase transformation to austenite is completed by the heating process, and the complete forward phase transformation is acquired by the cooling process. The larger ini-

tial strain of SMA film, the higher magnitude of actuating force can be generated. The hysteretic curves of recovery stress are observed with the thermal cycle. Moreover, these hysteretic characteristics of SMAs should be carefully considered to control precision shape of the structure by using SMA film actuators.

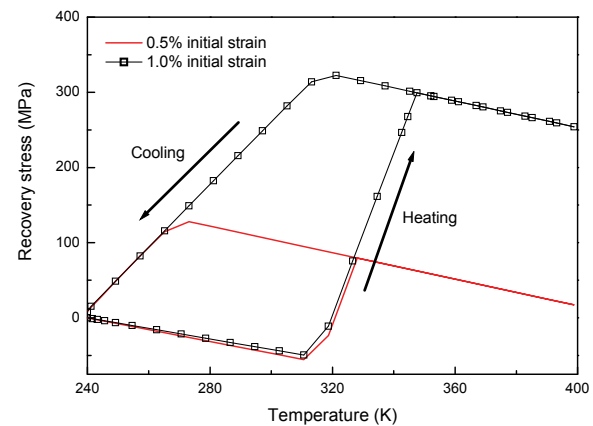


Figure 10: Hysteresis of recovery stress with thermal cycle

#### 4 Configuration Maintenance

Inflated membrane structures are faced with many challenges, particularly the need to achieve and maintain precise shape. Therefore, the reliable maintenance of the shape or surface precision during the mission life is one of the most important technologies for the demonstration of inflatable structures. In this section, a methodology to correct local deviations in the shape of the inflated membrane structures with SMA film actuator is numerically examined. A simple methodology to shrink or stretch sections of the membrane or the support structure is applied. By coupling two numerical algorithms of wrinkling and SMA film, the interactions between the inflatable structure and the SMA film actuator are investigated.

An inflatable antenna is comprised of two basic structures: the inflatable reflector assembly and a torus / strut supporting structure seen from Fig. 11 [Freeland et al (1993)]. To demonstrate configuration control, two inflatable membrane structures, each with SMA film are used: (1) an inflat-

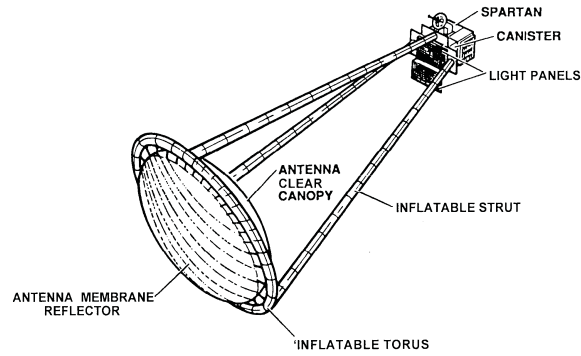


Figure 11: Inflatable antenna configuration

able boom similar to a strut supporting structure and (2) an inflatable reflector, which is comprised of two inflated membranes and torus supporting structures.

#### 4.1 An Inflatable boom with SMA film

An inflatable boom is used as a support structure for space inflatable antenna. The support structure, such as the inflatable boom, is rigidized after its deployment. In this study, it is assumed that the boom undergoes inflation. A numerical model for a membrane boom structure with SMA film is illustrated in Fig. 12. The membrane structure and the SMA film are modeled using 693 and 33 membrane elements (M3D4), respectively (ABAQUS [Hibbitt et al. (2003)]). SMA film with a width of 6mm is adhered on the surface of the structure. The thermomechanical properties of the SMA film are the same as those in Table 1. The membrane boom is made of Kapton film [DuPont Company], and its geometry and material properties are summarized in Table 2.

Table 2: Geometry and material properties of the inflatable boom

Modulus ( $E$ )	2.5 GPa
Poisson's ratio ( $\nu$ )	0.34
Coefficient of Thermal Expansion ( $\alpha$ )	$20 \times 10^{-6}/^{\circ}\text{C}$
Thickness ( $t$ )	$25 \times 10^{-6}\text{m}$
Length ( $L$ )	0.95m
Diameter ( $D$ )	0.19m

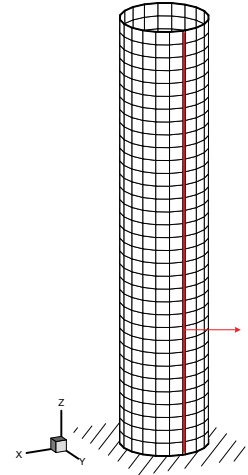


Figure 12: An inflatable boom structure with SMA thin film

The SMA film has an initial strain in the  $z$ -direction. When the SMA film is activated by raising its temperature above the austenite start temperature, strain recovery in the activated SMA film causes structure to bend due to its off-center location. Figure 13 shows the tip deflection versus temperature variation on the SMA film with internal pressure of 3,447Pa (0.5psi) and 2% initial strain on film. To show the wrinkling effect on the structure, two numerical results are compared. Temperature increases from initial temperature of 20°C. Tip deflections decrease at the initial temperature increment range due to the thermal expansion effect. However, starting from around the austenite temperature ( $A^{0s} = 39^{\circ}\text{C}$ ), the deflection starts to increase. Moreover, when the wrinkling effect is considered, the deflection increases rapidly at a critical temperature. This critical collapse point is induced by the recovery strain of the SMA film. At a temperature close to 65°C, the inflated boom collapses the by wrinkling development, which must avoid for structural performance when SMA film actuator is used.

Figure 14 shows the tip deflection in the case of 2% initial strain of SMA film at internal pressure, 3,447 and 6,895Pa. As shown in the figure, the critical collapse temperature increases with increasing internal pressure. The hysteresis loops for tip deflections versus the thermal cycle on SMA film with initial strains of 0.5% and 2% are

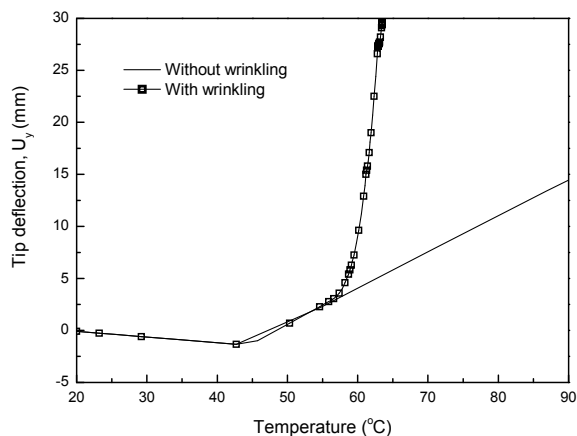


Figure 13: Wrinkling effect on the tip deflection

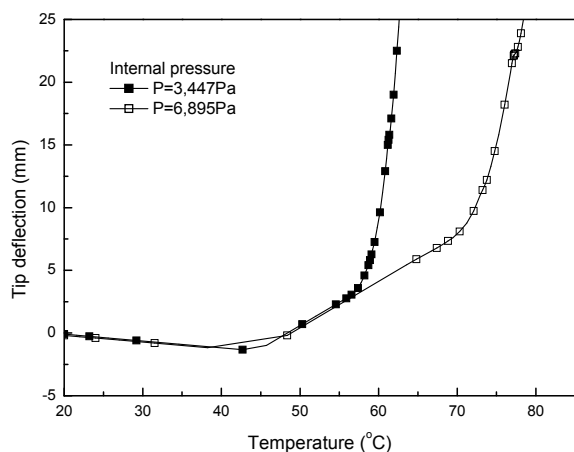


Figure 14: Tip deflection at various internal pressure

illustrated in Fig. 15. The deformed shape cannot be fully recovered at the end of the first thermal cycle because the elastic energy of the host membrane structure is not sufficient to recover the deformed strain of the SMA film. Accordingly, the deformed configuration of the boom during the heating process dose not change and further deflection is induced by the thermal expansion effect of the SMA film after the first thermal cycle. It is difficult to design a perfectly reversible membrane structure using an one-way SMA film. Two-way shape memory can be a solution to make the actuation reversible. However, if high precision is needed in terms of activation magnitude versus the number of cycles, the issues of thermal drift in the response are still not completely re-

solved. Therefore, the accurate prediction of the interactions between the inflated membrane structures and the SMA film should be further studied to design an actuator and a shape adaptive inflatable structure, taking into account the nonlinear and hysteretic behaviors of the membrane and SMAs.

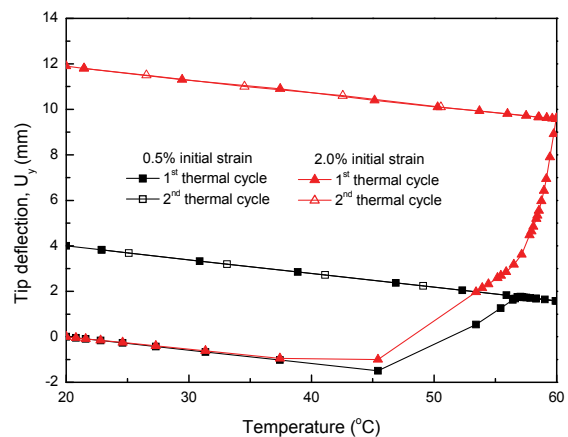


Figure 15: Hysteresis of tip deflections with various initial strains of SMA film

The maintenance of precise configuration under a thermal environment is investigated to show the effectiveness of SMA film actuator. It is assumed that the surface where the SMA thin film is bonded is subjected to a thermal load of  $60^{\circ}\text{C}$  due to the solar radiation. However, the opposite surface is subjected to a thermal load of  $-80^{\circ}\text{C}$  due to shaded area. The temperature distribution of the inflatable boom structure is illustrated in Fig. 16. Internal pressure of  $3,447\text{Pa}$  ( $0.5\text{psi}$ ) is applied. The tip deflection without SMA film decreases due to the thermal load as shown in Fig. 17. However, when using SMA film, the tip deflection tends to recover from the thermally deformed position to the initial state beyond  $40^{\circ}\text{C}$ , which is around the austenite start temperature ( $A^{0s}=39^{\circ}\text{C}$ ) of the SMA film (Table 1). When  $0.5\%$  initial strain is applied, the tip deflection starts to increase at a temperature of around  $39^{\circ}\text{C}$  and decreases due to the thermal expansion effect once the temperature-induced phase transformation is completed.

For the case of applying  $1\%$  initial strain on the SMA film, the tip location returns to its origi-

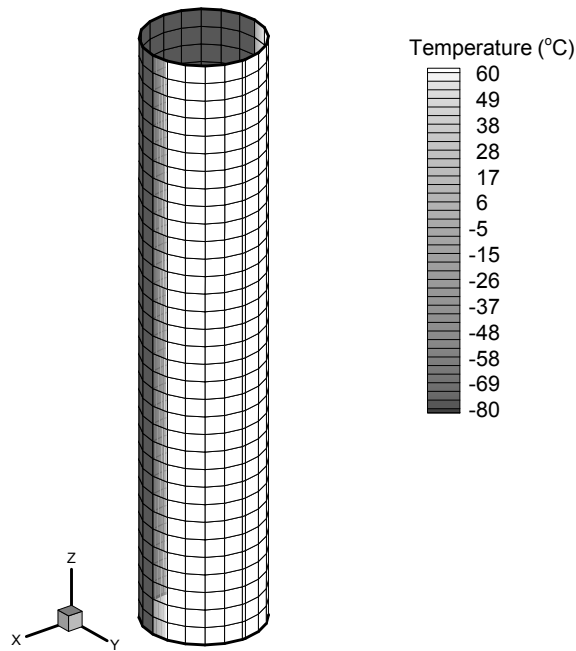


Figure 16: Temperature distribution of an inflatable boom structure

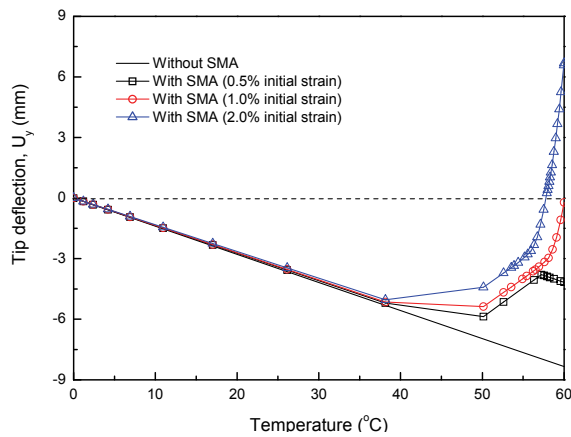


Figure 17: Shape effect of SMA film

nal location, and the deformation of the inflatable boom at 60°C is illustrated in Fig. 18. The deformation is concentrated near the area to which the SMA film is adhered. In addition, wrinkled areas develop as shown Fig. 19. By using SMA film with an 1% initial strain, the maintenance of the shape configuration of the inflatable boom structure could be possible. However, the negative effects on the structure are also observed due to recovery stress and strain of the SMA film: (1) the

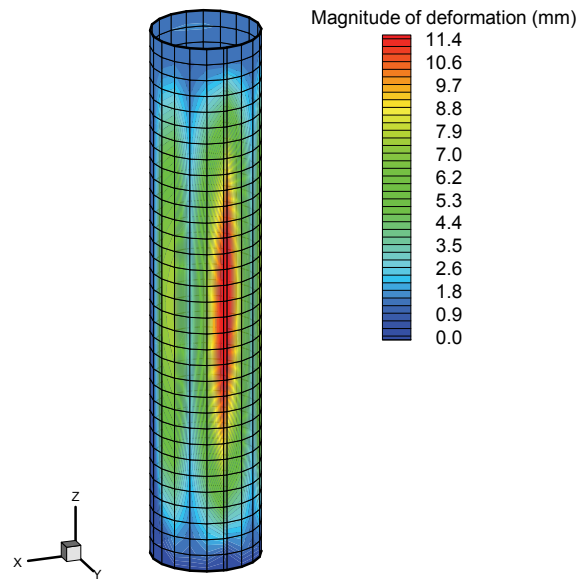


Figure 18: The deformation of inflatable boom at 60°C

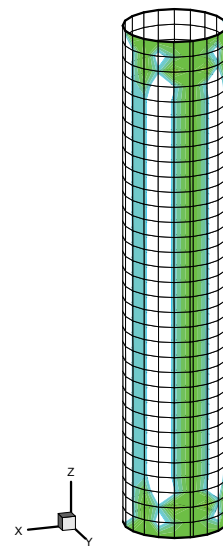


Figure 19: Wrinkling areas of inflatable boom at 60°C

deformation is concentrated around the actuator and (2) wrinkled area develops.

In the case of using a 2% initial strain, the tip location is excessively offset from its original location due to excessive recovery strain of the SMA film. The excessive offset also depends on internal pressure of the membrane structure. Hence, an optimal design process should be developed for

the accurate position control and structural performance by determining the recovery strain of SMA film, which depends on internal pressure or environmental temperature difference.

#### 4.2 An Inflatable reflector with SMA film

For a second demonstration of maintaining a precise surface configuration, an inflatable reflector with an SMA film is investigated. Figure 20 shows the schematics of the inflatable reflector with the SMA film to adjust the edge radial displacement. Two sheets of circular membrane are joined along their perimeters and the enclosed space between them is pressurized. One membrane serves as a canopy through which light is transmitted and the other serves as a reflector. The SMA film has an initial strain in the radial direction.

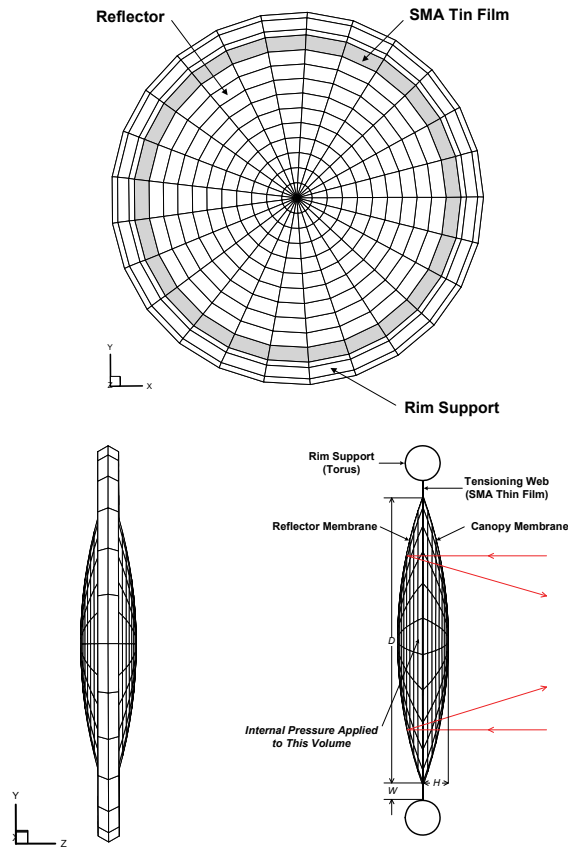


Figure 20: Schematics of the inflatable reflector with SMA film

When the SMA is activated by raising its tem-

perature above the austenite start temperature, the tension actuating force and displacement of SMA film can induce the central deflection change. Adjusting the edge radial displacement is particularly attractive due to the relative simplicity of its implementation. The reflector is initially designed to take the form of a spherical cap when internal pressure,  $P$  is applied. The diameter of the membrane is denoted as  $D$ , the center height as  $H$  and the width of the SMA film as  $W$ . The support structure, such as a torus (rim support), is rigidized after deployment. However, the reflector, such as lenticular structure, is purely inflatable. The torus structure is assumed as a rigid body. The reflector and canopy is made of Kapton film [DuPont Company] and its geometry and material properties are shown in Table 3. The applied thermomechanical properties of the SMA film are given in Table 1. For the numerical model, the reflector is modeled using 475 membrane elements (M3D4 and M3D3), and the thin film of SMA is modeled using 25 membrane elements (M3D4) by ABAQUS [Hibbitt et al. (2003)].

Table 3: Geometry and material properties of the inflatable reflector

Thickness ( $t$ )	$25 \times 10^{-6}\text{m}$
Diameter ( $D$ )	4.0m
Center Height ( $H$ )	0.35m
Width of SMA thin film ( $W$ )	0.2m
Modulus ( $E$ )	2.5 GPa
Poisson's ratio ( $\nu$ )	0.34
Coefficient of Thermal Expansion ( $\alpha$ )	$20 \times 10^{-6}/^{\circ}\text{C}$

The center displacement change of the inflatable reflector surface induced by radial tension of the SMA film is investigated. Internal pressure of 138Pa (0.02psi) is applied. This value of internal pressure is very small compared with that of the inflatable boom 3,447Pa (0.5psi). Note that the required inflation pressure is very low, and is inversely proportional to the size of the reflector. For example, the In-Space Technology Experiments Programs (IN-STEP), where the diameter of the reflector is 14m, the inflation pressure of

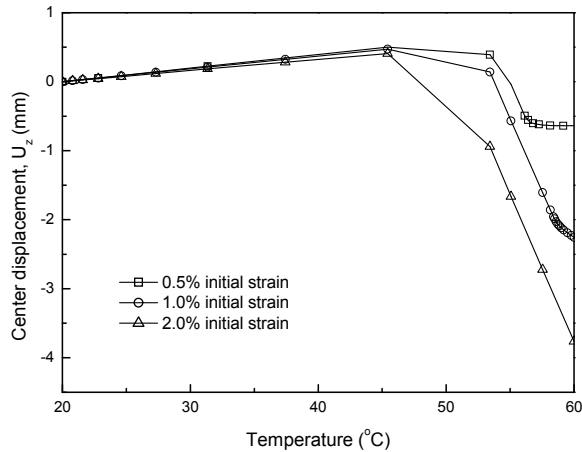
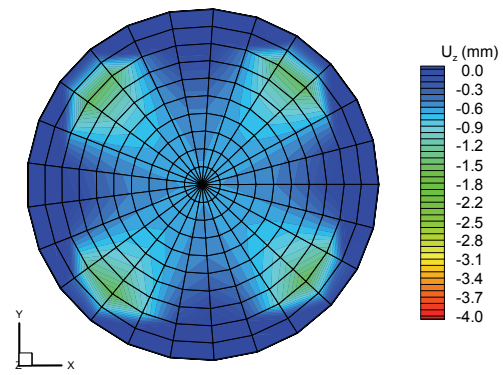


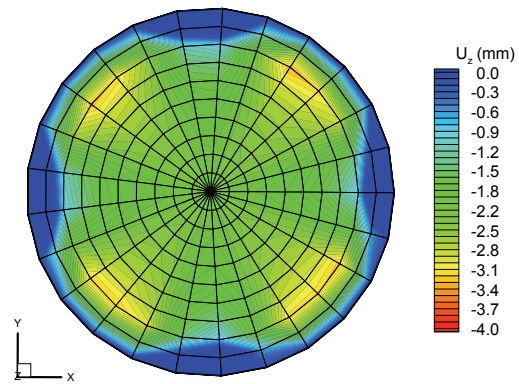
Figure 21: Vertical displacement vs. temperature for various initial strains

2.1Pa ( $3 \times 10^{-4}$ psi) is applied [Gordon and Robert (1995)]. Figure 21 shows that the vertical displacement induced recovery strain of the SMA film in the radial direction. It is found that this proposed concept of adjusting the edge radial displacement with SMA film is effective controlling the surface configuration. The deviation of the deformed shape from the inflated configuration with various initial strains of the SMA film at 60°C is illustrated in Fig. 22.

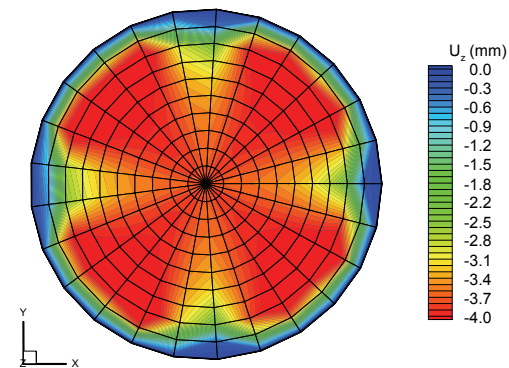
The maintenance of surface configuration under a thermal environment is investigated to show the effectiveness of SMA film for adjusting the edge radial displacement. It is assumed that the temperature of the reflector surface is 60°C due to solar radiation, but that of the canopy surface is -80°C due to shadow area. The deformed shape of the canopy is not considered because its function is merely to transmit the light. Figure 23 shows the effectiveness of the SMA film for maintenance of surface configuration under a thermal environment. As can be seen, the center vertical deflection is effectively controlled by adjusting the radial edge displacement using an SMA thin film. In addition, each deformed surface configuration at 60°C is illustrated in Fig. 24. However, in the cases using 2% and 4% initial strain of the SMA film, a wrinkled area develops due to the excess radial displacement change, which induces a compression stress combined with in-



(a) 0.5% initial strain of SMA



(b) 1.0% initial strain of SMA



(c) 2.0% initial strain of SMA

Figure 22: Deformed shape due to tension of SMA thin film at 60°C

ternal pressure. The developed wrinkling area at 60°C is illustrated in Fig. 25. The wrinkling development on the reflector surface could cause serious problems with the accuracy of reflector. Therefore, such wrinkling development should be prevented, and an optimal design process is necessary to maintain the reflector surface accurately under a thermal environment.

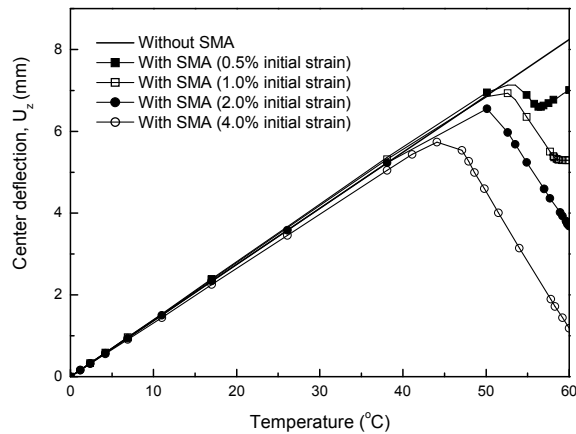


Figure 23: Vertical displacement with temperature variation

The internal pressure is changed to half that of the previous case to 69Pa (0.01psi). The effectiveness of an SMA film for maintenance of surface configuration under a thermal environment is illustrated in Fig. 26. Furthermore, the center vertical deflection can be effectively controlled by adjusting the radial edge displacement using an SMA film. With no SMA film, a wrinkled area develops at 60°C by thermal gradient. By increasing the initial strain of the SMA film, the developed wrinkled area could be reduced as shown in Fig. 27. However, for 3% initial strain of the SMA film, the wrinkled area develops further than that of other initial strains of the SMA film due to the excess radial displacement change, which induces compression combined with internal pressure.

### 5 Conclusion

A methodology for maintaining the surface configuration of an inflatable structure using shape memory alloy (SMA) film actuators has been numerically investigated in this paper. To understand the nonlinear behaviors of an inflated membrane structures due to wrinkling, the numerical model of inflated membrane boom is developed by applying the Stein-Hedgepeth membrane theory. The deformed shape and wrinkling development are numerically observed and there are very good correlations with experimental results. The two dimensional incremental formulation of the SMA constitutive model is proposed to predict the

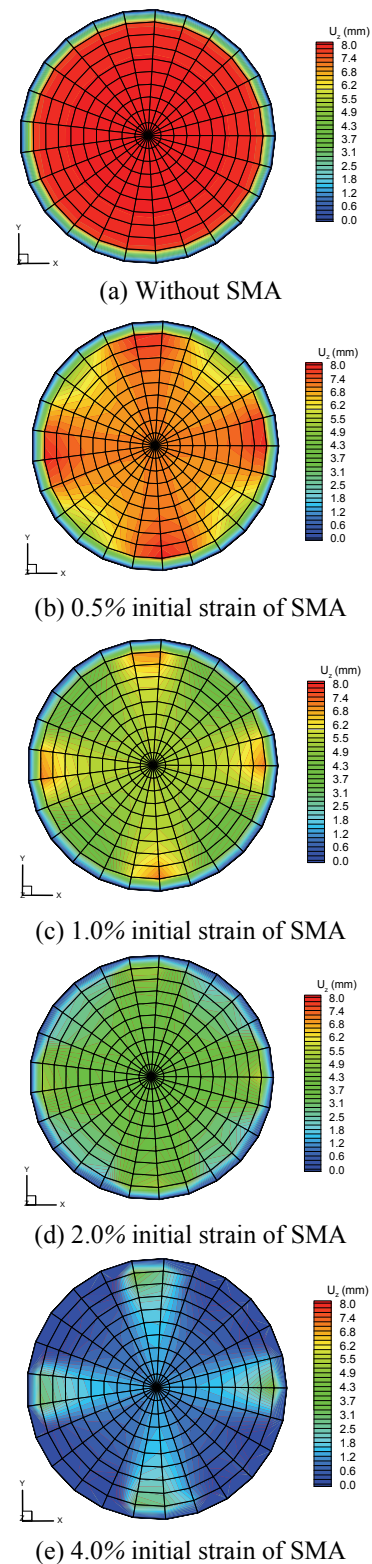
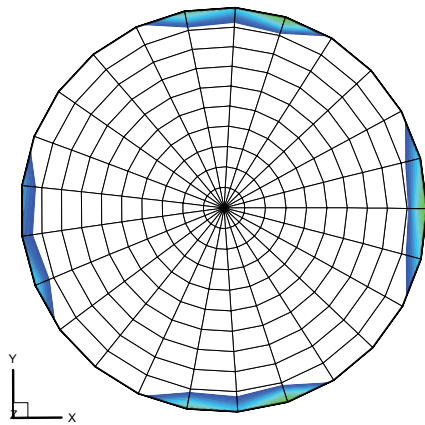
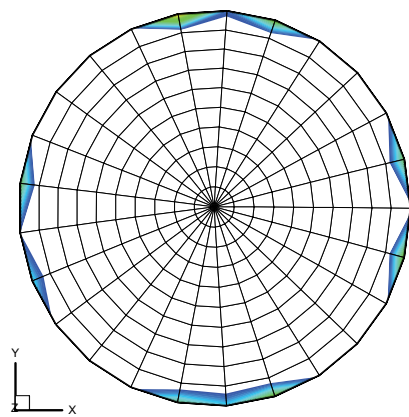


Figure 24: Deformed surface configurations of reflector at 60°C



(a) 2.0% initial strain of SMA



(b) 4.0% initial strain of SMA

Figure 25: Developed wrinkled areas at 60°C

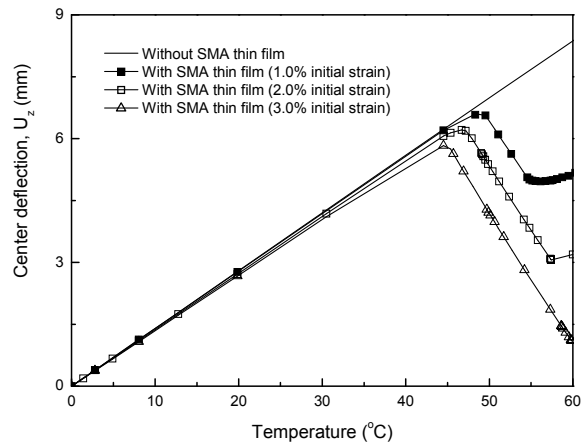
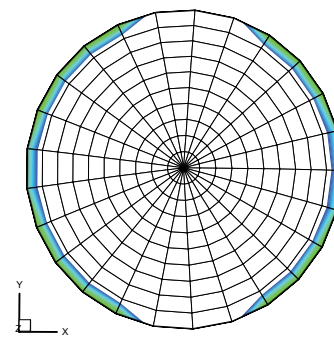
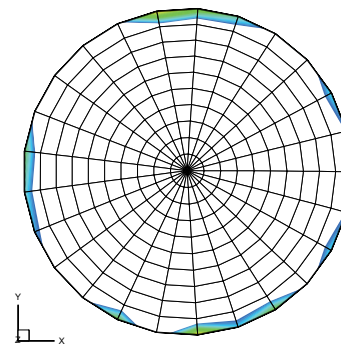


Figure 26: Vertical displacement with temperature variation

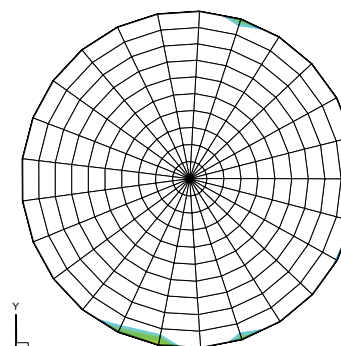
thermomechanical responses of SMA film actuators. For two dimensional problems, the general



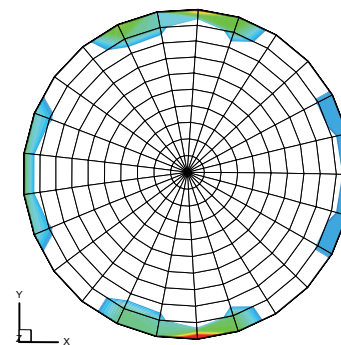
(a) Without SMA film



(b) 1% initial strain of SMA



(c) 2% initial strain of SMA



(d) 3% initial strain of SMA

Figure 27: Wrinkled areas at 60°C

expression derived in the Lagoudas model is modified into a plane stress condition. Moreover, new parameters that account for the thermodynamic energy are introduced to describe more general behaviors of the SMA film. The proposed SMA model shows a good prediction for the hysteresis of the strain-stress curve.

A simple methodology to shrink or stretch sections of the membrane or support structure is applied to maintain the accurate configuration of inflated membrane structures. By coupling the two numerical algorithms, for wrinkling and for film of SMA, the interactions between the inflatable structures and SMA film actuators are investigated. For the configuration control, two inflatable membrane structures, such as an inflatable boom and reflector, are demonstrated. It is found that the thin film of SMA is very effective to control the deflection position and configuration. However, negative effects, such as offset from initial configuration or development of a wrinkling area, could be induced by excessive recovery strain of the SMA film. Therefore, an optimal design process is needed to maintain accurate position and surface configuration by determining a proper recovery strain of SMA film, depending on the internal pressure or the environmental temperature difference. The accurate prediction of the interactions between inflated membrane structures and an SMA film should be further studied to design an actuator and a shape adaptive inflatable structure, taking into account the nonlinear and hysteretic behaviors of the membrane and SMAs.

**Acknowledgement:** This work was supported by the second state of the Brain Korea 21 Project in 2007. The authors also acknowledge the support by the Korea Research Foundation Grant funded by the Korean Government (MOEHRD) (KRF-2007-357-D00045).

## References

**Stein, M.; Hedgepeth, J. M.** (1961): Analysis of Partly Wrinkled Membranes, Technical Note, NASA TN D-813.

**Miller, R. K.; Hedgepeth, J. M.; Weingarten, V. I.; Das, P.; Kahyai, S.** (1985): Finite Element Analysis of Partly Wrinkled Membranes, *Computers & Structures*, Vol. 20, No. 1-3, pp. 631-639.

**Freeland, R. E.; Bilyeu, G. D.; Veal, G. R.** (1993): Validation of a Unique Concept for a Low-Cost, Lightweight Space-Deployable Antenna Structure, URL: <http://www.lgarde.com/papers/iaf-93-i-1-204.pdf>.

**Salama, M.; Kuo, C. P.; Garba, J.; Wada, B.; Thomas, M.** (1994): On-Orbit Shape Correction of Inflatable Structures, URL: <http://www.lgarde.com/papers/94-0306.pdf>.

**Gordon, V.; Robert, F.** (1995): In-Step Inflatable Antenna Description, URL: <http://www.lgarde.com/papers/aiaa-95-1193b.pdf>.

**Lexcellent, C.; Moyne, S.; Ishida, A.; Miyazaki, S.** (1998): Deformation Behaviour Associated with the Stress-Induced Martensitic Transformation in Ti-Ni Thin Films and Their Thermodynamical Modelling, *Thin Solid Films*, Vol. 324, pp. 184-189.

**Kang, S.; Im, S.** (1999): Finite Element Analysis of Dynamic Responses of Wrinkling Membranes, *Computer Methods in Applied Mechanics and Engineering*, Vol. 173, pp. 227-240.

**Wagner, J. W.; Agnes, G. S.; Magee, E.** (2000): Optical Metrology of Adaptive Membrane Mirrors, *Journal of Intelligent Material Systems and Structures*, Vol. 11, No.11, pp. 837-847.

**Qidwai, M. A.; Lagoudas, D. C.** (2000): Numerical Implementation of a Shape Memory Alloy Thermomechanical Constitutive Model using Return Mapping Algorithms, *International Journal for Numerical Methods in Engineering*, Vol. 47, pp. 1123-1168.

**Lewis, J. A.; Inman, D. J.** (2001): Finite Element Modeling and Active Control of an Inflated Torus Using Piezoelectric Devices, *Journal of Intelligent Material Systems and Structures*, Vol. 12, No. 12, pp. 819-833.

**Jenkins, C. H.; Schur, W. W.** (2002): Gore/Seam Architectures for Gossamer Structures, *Journal of*

*Spacecraft and Rockets*, Vol. 39, No. 5, pp. 669-673.

**Duvvuru, H.; Hossain, A.; Jenkins, C. H.** (2003): Modeling of an Active Seam Antenna, *Proceeding of the 44<sup>th</sup> AIAA/ASME/ASCE/AHS/ASC Structures, Structural Dynamics & Materials Conference*, Norfolk, VA.

**Flint, E. M.; Denoyer, K. K.** (2003): Approach for Efficiently Evaluating Internally Reacted Global Shape Control Actuation Strategies for Apertures, *Proceeding of the 44<sup>th</sup> AIAA/ASME/ASCE/AHS/ASC Structures, Structural Dynamics & Materials Conference*, Norfolk, VA.

**Hibbitt, H. D.; Karlson B. I.; Sorenson, E. P.** (2003): *ABAQUS User's Manual*, HKS Inc., RI Version 6.4.

**Woo, K.; Igawa, H.; Jenkins, C.H.** (2004): Analysis of Wrinkling Behavior of Anisotropic Membrane, *CMES: Computer Modeling in Engineering and Sciences*, Vol. 6, No. 4, pp. 397-408.

**Roh, J. -H.; Han, J. -H.; Lee, I.** (2006): Nonlinear Finite Element Simulation of Shape Adaptive Structures with SMA Strip Actuator, *Journal of Intelligent Material, Systems and Structures*, Vol. 17, No. 11, pp. 1007-1022.

**Yoo, E. -J.; Roh, J. -H.; Han, J. -H.** (2007): Wrinkling Control of Inflatable Booms Using Shape Memory Alloy Wires, *Smart Materials and Structures*, Vol. 16, No. 2, pp. 340-348, 2007.

**DuPont Company** (<http://www.dupont.com>).